QUARTERLY JOURNAL OF THE ROYAL METEOROLOGICAL SOCIETY
RMetS Royal Meteorological Society

Convective updraught evaluation in high-resolution NWP simulations using single-Doppler radar measurements

Journal:	*QJRMS*
Manuscript ID:	Draft
Wiley - Manuscript type:	Research Article
Date Submitted by the Author:	n/a
Complete List of Authors:	Nicol, John; University of Reading, Department of Meteorology Hogan, Robin; University of Reading, Meteorology; Stein, Thorwald; University of Reading, Department of Meteorology Hanley, Kirsty; MetOffice@Reading, Clark, Peter; University of Reading, Meteorology Halliwell, Carol; MetOffice@Reading, Lean, Humphrey; MetOffice@Reading, Plant, Robert; University of Reading, Meteorology
Keywords:	Numerical Weather Prediction, convective updraught, vertical velocities, grid length, single-Doppler radar retrievals, sub-grid turbulence

Convective updraught evaluation in high-resolution NWP simulations using single-Doppler radar measurements

Nicol JC[a], Hogan RJ[b], Stein THM[b], Hanley KE[c], Clark PA[b], Halliwell CE[c], Lean HW[c] and Plant RS[b]

[a] National Centre for Atmospheric Science (NCAS), University of Reading, Reading, UK

[b] Department of Meteorology, University of Reading, Reading, UK

[c] MetOffice@Reading, Reading, UK

ABSTRACT:

This study presents an evaluation of the size and strength of convective updraughts in high-resolution simulations by the UK Met Office Unified Model (UM). Updraught velocities have been estimated from range height indicator (RHI) Doppler velocity measurements using the Chilbolton advanced meteorological radar; collected as part of the Dynamical and Microphysical Evolution of Convective Storms project (DYMECS). Based on mass continuity and the vertical integration of the observed radial convergence, vertical velocities tend to be underestimated for convective clouds due to the undetected cross-radial convergence. Velocity fields from the UM at a resolution corresponding to the radar observations are used to scale such estimates to mitigate the inherent biases. The analysis of more than 100 observed and simulated storms indicates that the horizontal scale of updraughts in simulations tend to decrease with grid length; the 200-m grid length agreed most closely with the observations. Updraught mass fluxes in the 500-m grid length simulations were found to be up to an order of magnitude greater than were observed; even greater mass fluxes were produced in the 1.5-km grid length simulations. The effect of increasing the mixing length in the sub-grid turbulence scheme depends on the grid length. For the 1.5-km simulations, updraughts were weakened though their horizontal scale remained largely unchanged, being determined primarily by the grid length. Progressively more so for the sub-kilometre grid lengths, updraughts were broadened and intensified; horizontal scale was now determined by the mixing length rather than the grid length. These tendencies were reversed with decreased mixing lengths. The findings in terms of updraughts were supported by the analysis of the widths of monotonically decreasing reflectivity patterns in both the simulations and observations. In general, simulated updraughts tended to weaken too quickly with height; future work will investigate possible dynamical and microphysical causes.

Keywords: Numerical Weather Prediction, grid length, convective updraught, single-Doppler radar retrievals, vertical velocities, sub-grid turbulence

1. INTRODUCTION

Accurate forecasting of convective rainfall is of great importance with respect to severe weather and flash flooding; however, the high spatial and temporal variability make this very challenging and difficult to parameterize in forecast models. Several operational forecast centres now run Numerical Weather Prediction (NWP) models at convection-permitting grid lengths of the order 1 km with no convective parameterization (e.g., Lean *et al*., 2008; Baldauf *et al*., 2011). Even then, NWP models can have difficulty resolving convective processes; the resulting storms can develop/evolve too slowly, be too intense when mature and may lack mesoscale organization (e.g., Weisman *et al*., 1997; Bryan and Morrison, 2012; McBeath *et al*., 2013; Hanley *et al*., 2014). Convective updraught scale and strength are fundamental to the microphysical development of the resulting rainfall and must be suitably represented in NWP models. The evaluation of high-resolution forecast models is typically limited to the analysis of surface precipitation or (forward-modelled) radar reflectivity fields (e.g., Kain *et al*., 2008; Varble *et al*., 2011; Caine *et al*., 2013). However, to improve the representation of rainfall of convective origin in NWP requires a better understanding of how updraughts are represented.

Methods of directly observing vertical air motion in convective clouds are extremely limited. Although wind profilers can directly provide updraught statistics (e.g. May and Rajopadhyaya, 1999), the spatial representativity of these observations is an important issue as they only detect clouds air motions passing directly over the profiler site. In contrast, indirect observations such as those based on dual- or multi-Doppler radar retrievals can provide good spatial coverage, though are subject to many sources of error and require some form of constraint, such as through variational approaches and the minimization of cost functions (e.g., Scialom and Lemaitre, 1990; Bousquet and Chong, 1998; Gao *et al*., 1999). These approaches show great potential, if

significant care is taken at each step in the data collection and processing, and in the constraints applied (e.g., Collis *et al*., 2013). However, such observations have yet to be made extensively and over a broad range of climatic conditions. This is primarily due to the limited overlap of Doppler radar observations in operational networks and the limited number of case studies afforded dual- or multi-Doppler coverage. Future studies with extensive multi-Doppler coverage provide the greatest potential to accurately evaluate the representation of vertical air motion in NWP models.

Field studies involving the deployment of portable Doppler radars for this purpose in the United Kingdom are extremely rare, so other approaches are required. The COnvective Precipitation Experiment (COPE) was one recent exception in summer 2013 though even then, the extent of dual-Doppler coverage was very limited (Blyth *et al.*, to be submitted to BAMS January 2015). The Dynamical and Microphysical Evolution of Convective Storms project (DYMECS; Stein *et al*., in revision for *BAMS*) involved the automated tracking of convective storms over 40 days using observations from the operational radar network to direct automated volume scans and vertical cross-sections (RHIs) through the most active convective storms using the Chilbolton Advanced Meteorological Radar (CAMRa; Goddard *et al*., 1994a). The initial focus of DYMECS was to compare the morphology of convective storms in high-resolution simulations with the Met Office Unified Model (UM) against these observations (Stein *et al*., 2014) and to investigate mixing length controls in the sub-grid turbulence scheme used in these simulations of convective storms based on the analysis of surface rainfall fields (Hanley *et al*., 2014). Here, we present a study of the representation of updraught scale and strength in the UM using single-Doppler radar observations made during DYMECS.

Single-Doppler RHIs have previously been used for the estimation of streamlines and vertical air motion (Browning *et al*., 1997; Chapman and Browning, 1998; Browning *et al*., 2010; Crosier *et al*., 2014) based on the vertical integration of the radial component of convergence observed by radar. These studies have relied on the fact that the meteorological systems considered could be approximated as two-dimensional structures (e.g. associated with frontal rain bands or convergence lines); when orientated perpendicular to the radar beam axis, the cross-axis component of convergence may be neglected. However, such approximations are not valid for convective or cellular rainfall. Although the convergence detected along a single horizontal dimension may indicate where updraughts occur, one would not expect the true vertical velocity to be accurately represented. In this paper, we address this problem by analyzing the velocity fields from the UM at a comparable resolution to the radar observations, in order to determine how to scale the raw estimates to better represent the observed convective updraughts.

In section 2, we describe the radar observations and model simulations used here and outline the case studies considered. Section 3 presents the technique used for the estimation of vertical air velocities using single-Doppler radar observations, including a new approach for combining estimates using both the upward and downward integration of convergence, and a novel means of scaling the combined estimates based on the analysis of simulated wind fields. In section 4, the representation of convective updraughts in the UM is investigated as a function of horizontal grid length and dynamical and microphysical parameterisations. Finally, conclusions are presented in section 5.

2. OBSERVATIONAL AND MODEL DATA

2.1 Radar observations

The radar observations presented in this work were made using CAMRa, a 3-GHz (S-band) dual-polarization Doppler radar located at Chilbolton in Southern England. This radar is regularly calibrated with an anticipated accuracy of ~0.5 dB (Goddard *et al*., 1994b). The large 25-m dish provides high spatial resolution (0.28° beamwidth; ~440 m at 90 km) and high sensitivity (minimum detectable signal ~ -5 dBZ at 90 km). In this study, the maximum range for the centre of any rain cells considered was set to 90 km to limit the dimensions of the beam, the sensitivity of the radar and the height of the beam above the ground. The minimum elevation clear of beam blocking is ~0.5° at most azimuths, at which the centre of beam has a height above ground of ~1.23 km at 90 km. However, considering that the Doppler velocity may still be used in regions with partial beam blocking, observations much closer to the ground were available even out to this range.

A real-time storm-tracking and scan-scheduling procedure was developed for DYMECS which automatically steers the radar towards storms of interest, which were identified from the surface rainfall composite provided by the UK operational radar network. The prioritization of storms was updated every 5 minutes based on many factors such as storm size, intensity, persistence and location relative to the radar. Greater preference was typically given to storms at ranges between about 40 and 100 km. A detailed description of the cell tracking, prioritization and scanning procedures is provided by Stein *et al*. (2014). While the scan scheduling was primarily intended for the later construction of storm volumes from closely stacked PPIs in narrow sectors, additional RHI scans were collected along azimuths dissecting the reflectivity maxima of the prioritized storms, taking the observed advection of the storm into account. RHIs directed through up to three individual storms were made every 10 to 15 minutes, resulting in the sampling of over 50 storms for each of the case studies later presented.

2.2 The Met Office Unified Model

The UM is the operational NWP model used by the Met Office to provide global and regional deterministic and ensemble forecasts. The model solves non-hydrostatic, deep-atmosphere dynamics using a semi-implicit, semi-Lagrangian numerical scheme (Davies *et al*., 2005). A detailed description of the model configuration used during the DYMECS project and the nested domain sizes may be found in Hanley *et al*. (2014). The horizontal grid lengths investigated in this work range from 1500 m (currently used for operational forecasting over the United Kingdom) down to 100 m. The model configuration corresponded in general to the operational settings at the time of the observational campaign (i.e. 2012). A common domain extending from 200 km West to 100 km East of Chilbolton and from 125 km South to 100 km North of the radar was used in the later analyses for all but the 100-m grid length simulations. Due to the computational expense of these simulations, a smaller domain was used running from 125 km West to 50 km East and from 75 km North to 75 km South relative to Chilbolton.

The vertical grid uses Charney-Phillipps staggering (Charney and Phillips, 1953) and a terrain-following hybrid-height vertical coordinate. The 1500 m grid length simulations use 70 vertical levels. This results in a spacing of ~150 m at 1 km above the ground and ~300 m at a height of 8 km. Simulations at finer horizontal grid lengths were made using 140 vertical levels, halving the vertical spacing relative to the 1500 m grid length simulations (i.e. ~75 m at 1 km and ~150 m at 8 km). Tests made using both 70 and 140 vertical levels with a 500-m grid length produced almost identical precipitation fields, while significant changes were observed when a 200-m grid length was used. Because of this, the use of 140 levels at 1500-m grid length was not considered necessary.

A Smagorinsky-type sub-grid turbulence scheme (Smagorinsky, 1963) was used in the UM simulations which takes the moist Richardson number into account to provide the 3D mixing (Halliwell, 2007), characterized by a single mixing length. While the operational configuration with a 1.5-km grid length uses 2D Smagorinsky mixing with a boundary layer scheme to provide the vertical mixing, 3D mixing has been applied uniformly here at all grid lengths. A comparison of results with these two approaches demonstrated little difference in terms of updraught widths at 1.5-km grid length. As such, results from the 2D scheme have not been included here. The default configuration uses a mixing- to grid-length ratio of 0.2, which is intended to act as a suitable trade-off between the intended filter operation and computational efficiency (Lilly, 1967). Hanley *et al*. (2014) provide further details on the implementation of this scheme, which primarily acts to mix the humidity, temperature and wind fields across adjacent grid boxes. In section 4, we investigate the influence of changing the mixing length on the representation of updraughts in the UM, excluding simulations at 100-m grid length (again due to the computational expense).

The UM uses a single-moment microphysics scheme (Wilson and Ballard, 1999) with mixing ratios of cloud ice and cloud liquid as prognostic variables along with prognostic rain. A diagnostic split between crystals and aggregates determines the precipitation in the ice phase. Although the UM provides an option for treating crystals and aggregates as separate prognostic variables, it has not been used in this study. More details on the microphysical set-up of the UM for this study may be found in Stein *et al*. (2014) along with a detailed description of the calculations used to forward model radar reflectivity in the UM, used extensively in later sections. In section 4, we investigate an aggregate-only treatment of the ice phase and the inclusion of prognostic graupel in simulations using a 200-m grid length.

2.3 DYMECS case studies

In this paper we focus on two contrasting case studies, selected from the DYMECS project to evaluate the representation of updraughts at mid-latitudes in the UM. The first case, for which we consider data collected between 1200 and 1600 UTC 25 August 2012, exhibited the deepest and most vigorous convection observed during the project, with echo-top heights reaching above 10 km. The second case study, between 1100 and 1600 UTC on 20 April 2012, represents a more typical case of convective showers, which like many DYMECS cases, exhibited moderate convection up to heights of ~5 km. The 0° C isotherm was at about 2.7 km and 1.0 km in these two cases respectively. These cases are typical of the 'large storm' and 'shower' classifications in the DYMECS study by Hanley *et al*. (2014).

3. ESTIMATING UPDRAUGHTS FROM SINGLE-DOPPLER OBSERVATIONS

In this section, we describe the estimation of vertical air motion based on the analysis of the horizontal wind field and the assumption of flow continuity. A new approach for combining estimates derived from upward and downward integrations based on the propagation of constant errors is presented. The limitations of implementing this approach using Doppler radar observations are discussed, specifically when only a single component of the horizontal wind is available. Finally, we present a novel means of scaling the estimates to allow for the missing component of horizontal convergence in a statistical sense. This is based on the analysis of horizontal wind fields derived from high-resolution numerical simulations using the UM.

3.1 Estimating vertical air motion in a column

The retrieval of vertical air motion using dual- or multi-Doppler radar observations is well established in the literature (e.g., Miller and Strauch, 1974; Ray *et al*., 1980). When orthogonal

components of the horizontal convergence are known throughout a vertical column, vertical velocities may be obtained by simply integrating local changes in the horizontal mass flux. This approach is based on the assumption of flow continuity accounting for density changes with height and requires at least one boundary condition with zero vertical velocity, either at the surface or at the echo top. Although the surface boundary condition is more exact if observations are available close to the ground, the choice of the direction of integration is confounded by the fact that any errors in the observed convergence are amplified when integrating upwards due to the decrease in air density with height (e.g. Ray *et al*., 1980). Conversely, such errors are damped when integrating downwards. Protat and Zawadzki (1999) proposed a linear combination of estimates made by integrating in each direction in the context of multi-Doppler retrievals (their Eq. 8). We propose a new approach of combining these estimates for which the weights, rather than varying linearly with height, are obtained from the expected propagation of errors throughout the column using a standard atmospheric density profile and the echo top height. These errors represent the combination of errors due to the undetected component of convergence and (to a lesser extent) in the measurement of the radial component of convergence. For simplicity, we consider the error (σ_0) at each height bin to be independent of height and that the errors introduced by the boundary conditions may be neglected. Using the upward integration as an example, the estimated error in the vertical velocity at each successive height bin (index i) is given by Eq. 1.

$$\sigma_i = \sqrt{\left(\frac{\sigma_{i-1}\rho_{i-1}}{\rho_i}\right)^2 + \sigma_0^2} \qquad (1)$$

Such calculations are iterated up to the echo-top height to provide the anticipated vertical velocity estimation errors. This approach has also been used to derive the errors in the downward

integration. The weighting coefficients (ω) applied to the top-down and ground-up vertical velocity estimates at each height bin are given in Eq. 2 and 3 respectively and are shown in Fig.1 for echo-top heights up to 12 km.

$$\omega_{up} = \frac{\sigma_{down}^2}{\sigma_{down}^2+\sigma_{up}^2} \quad (2)$$

$$\omega_{down} = \frac{\sigma_{up}^2}{\sigma_{down}^2+\sigma_{up}^2} \quad (3)$$

Expressed in Eq. 4, this approach provides the minimum error in the vertical velocity estimates at each height for any combination of the ground-up and top-down estimates based on the prescribed errors.

$$\sigma_{weighted-avg.} = \frac{\sigma_{down}\sigma_{up}}{\sqrt{\sigma_{down}^2+\sigma_{up}^2}} \quad (4)$$

Progressively with increasing echo-top heights, more weight is given to the top-down approach throughout the column for the error-weighted approach relative to the linear-weighted approach. An example of the estimation errors as a function of height is shown in Fig. 1b for an echo top of 12 km (normalized relative to the maximum error from the error-weighted approach). While the linear-average proposed by Protat and Zawadzki (1999) actually results in slightly larger errors than the top-down integration through much of the mid-to-upper troposphere, the error-weighted approach is always more accurate than either of the estimates based on a single direction of integration. The linear-average approach results in anticipated vertical velocity errors that are about 25% greater than for the error-weighted approach through the mid-troposphere in this case; decreasing to approximately 15%, 10% and 5% for echo-top heights of 10 km, 8 km and 6 km respectively.

3.2 Single-Doppler retrievals

Doppler velocities from RHIs (vertical cross-sections) made at low elevations (e.g. < 10°) have been used to estimate the horizontal wind, neglecting the component due to the terminal fall speed of precipitation and vertical air motion. Local convergence estimates are only likely to be biased by this assumption when significant changes in the vertical component occur over relatively short horizontal distances (e.g. over 500 m). More importantly however, single-Doppler observations only detect one component of the horizontal convergence, along the plane of the RHI. Estimates of vertical air motion based on single-Doppler observations therefore require that the 'missing' component of convergence is negligible. While some fraction of the total horizontal convergence is likely to be detected when present, it is likely to be underestimated in most instances.

We propose to use high-resolution model simulations to determine in a statistical sense how best to scale vertical velocity estimates derived from a single horizontal component of convergence. This does not require that the simulations represent the actual wind field at any given time, rather that realistic three-dimensional flows are represented and that the full range of vertical velocities likely to be encountered are encompassed. While it is unlikely that this approach could provide accurate reconstructions of the vertical wind field in every instance, the estimates should be unbiased, so in a subsequent statistical analysis in which many updraughts are composited, random errors will largely cancel. As such, the width of the composite updraughts may be expected to be representative.

3.3 Application to Unified Model simulations

The following methodology has been applied to UM simulations with a grid length of 500 m from 25 August 2012, replicating the application of this technique to radar data presented later. This case was selected amongst the DYMECS cases as the strongest updraughts with the greatest vertical extents were exhibited. Firstly, vertical cross-sections of the along-axis horizontal winds were extracted for both North-South and West-East orientations, intersecting the maximum surface rainfall rate of significant rain cells between 1200 UTC and 1600 UTC. For the case considered, there was a tendency for the convection to be organised in bands running in a SW-NE direction. Consequently, the analysis of the North-South and West-East cross-sections provided almost identical results. Significant rain cells (136 cells in total) were defined by rainfall rates greater than 4 mm hr^{-1} over an area of at least 10 km^2. These winds were averaged to uniform 250-m height intervals before vertical velocities were estimated by integrating the mass flux determined from the single horizontal component (along axis) of convergence from these cross-sections.

Figure 2a shows the frequency density functions (FDFs) in logarithmic units of the estimated vertical velocities (0.2 m s^{-1} quantisation) normalised at each 250-m height band obtained by top-down integration starting from the forward-modelled -5 dBZ echo tops. Corresponding estimates made by integrating upwards from 500 m above the ground are shown in Fig. 2b, clearly displaying the amplification of errors with height using this approach. The results presented in Fig. 2c were obtained by combining the top-down and ground-up approaches using the weights described in the previous section (see Fig. 1). Finally, the FDFs of the actual vertical velocities represented in the model are displayed in Fig. 2d. Comparing Fig. 2c and 2d, it is clear that the

estimates derived from a single component of the horizontal wind tend to underestimate the largest positive vertical velocities (updraughts).

For each 250-m height interval, the cumulative frequency density functions (CFDFs) of the vertical velocities estimated from a single component of convergence have been mapped to the CFDFs of the actual velocities in the simulations over all the storms. This is depicted by the black trace in Fig. 3a for the height interval from 6 to 6.25 km. Vertical velocities have been estimated from the radar data collected on 25 August 2012. The mapping function depicted in Fig. 3a has then been used to scale these radar estimates to provide a best estimate of the true vertical velocities from the radar observations. A comparison of the results from model simulations and radar observations is presented in Fig. 3b for the same height interval. The black dashed and solid traces in Fig. 3b correspond to the results shown in Fig. 2c and 2d respectively at this height, depicting FDFs of the single-component estimates and the actual vertical velocities from the simulations. The grey dashed trace represents the vertical velocities estimated directly from the radar data, showing close agreement with the simulations. The resulting FDF of the scaled vertical velocities from the radar data are shown by the solid grey trace in Fig. 3b. Because such close agreement was found between the single-component estimates from the simulations and the radar in this case, the scaled radar estimates also show very good agreement with the actual velocities from the simulations.

Figures 4a-c correspond directly to Figs. 2a-c, though are derived from the radar data rather than the model simulations; that is they represent the FDFs of top-down and ground-up estimates and their weighted average respectively. Using the approach described above to scale the radar estimates from a single component of convergence (Fig. 4c), provides the FDFs of the 'best-estimates' of the true vertical velocities using the radar observations (Fig. 4d). A vertical velocity

retrieval is shown in Fig. 5a along with the corresponding reflectivity measurements (Fig. 5b) from an RHI taken at 1237 UTC 25 August 2012.

Based on the cross-section through all the storms in the 500-m simulations, a point-by-point comparison between the *true* vertical velocities and retrievals based on a single component of convergence gave a correlation of 0.72 and a root-mean-square (rms) difference of 1.2 m s^{-1}. Considering only points with significant estimated updraughts (i.e. > 1 m s^{-1}) provided a correlation of 0.73 and rms difference of 2.6 m s^{-1}.

4. THE REPRESENTATION OF UPDRAUGHTS IN THE UNIFIED MODEL

In this section, we shall consider vertical cross-sections of the vertical velocity and the forward-modelled reflectivity (also represented at uniform 250-m height intervals after linear averaging) from UM simulations. Orthogonal (North-South and East-West) cross-sections intersecting the maximum surface rainfall rate of significant convective rain cells have been extracted. An analysis of the rain cells sampled by the radar for each of the two case studies indicated that the area-integrated rainfall (AIR) for the vast majority of these rain cells corresponded to the top 50% AIR from the population, as derived from the operational radar network. To improve the representativity of the comparison between the simulations at various grid lengths and with the observations, we only consider rain cells for which the AIR was greater than the median AIR from any given population in the following analyses.

The maximum vertical velocity (w) and reflectivity (Z) associated with each of the rain cells considered have been determined at each height interval. These have been averaged to produce the profiles shown in Fig. 6, conditioned on the number of significant updraught detections at each height (also shown) for both the radar observations and model simulations. Significant

detections are defined when $Z > 100$ mm^6 m^{-3} (≡20 dBZ) and $w > 1$ m s^{-1}. For each of the two case studies, model simulations correspond to the default configurations with grid lengths of 1500 m, 500 m, 200 m and 100 m.

For 25 August 2012, the 1500-m grid length simulations have significantly weaker velocities, while for other grid lengths these velocities are remarkably similar to each other and to the observations in the lowest 3 km. The vertical velocities peak between 3 and 4 km in the simulations and then decrease steadily with height. In contrast, the observations show a steady or even slightly increasing velocity profile up to about 8 km before decreasing rapidly. The forward-modelled reflectivities in the simulations show reasonable agreement with the observations, although both the 100-m and 200-m grid length simulations tend to exhibit weaker peak reflectivities at low levels.

Both the vertical velocities and the forward-modelled reflectivities tended to be much weaker in the simulations than in the observations for 20 April 2012. Again, vertical velocities were weakest in the 1500-m simulations though tended to decrease in the higher resolution simulations at heights above about 1 km. In contrast, the radar-derived updraught strength peaked between 2 and 3 km. In this case, simulated reflectivities were significantly less than in the observations, particularly above the 0° C isotherm. Interestingly in both cases, the simulated vertical velocities displayed a decrease with height above the 0° C isotherm while in the observations the updraughts remained steady or even strengthened up to about 80% of the echo-top height.

4.1 Influence of model grid length

At each 250-m height interval, horizontal profiles of the vertical velocity and reflectivity associated with each rain cell have been extracted. Vertical velocity (w) and reflectivity (Z) values with $w < 1$ m s^{-1} or $Z < 100$ mm^6 m^{-3} (≡20 dBZ) were set to zero. These profiles were then centred on the maximum velocity or maximum reflectivity respectively for each rain cell at each height to produce mean w and Z profiles as a function of distance from the maximum. This avoids any broadening of the profiles when the vertical velocity and reflectivity maxima do not coincide.

The mean profiles of vertical velocity and reflectivity from 25 August 2012 are shown in Fig. 7 for the radar observations and for the default configurations of the various model grid lengths considered. The black horizontal bars at each 1-km height interval show the mean profile width of the updraught and reflectivity cores defined between thresholds of 1 m s^{-1} and 20 dBZ respectively. The apparent width of the mean reflectivity profiles (colour profiles) is generally greater than that represented by the horizontal bars as it can be unduly influenced by an occasional strong profile due to the linear averaging of reflectivity (in mm^6 m^{-3}). As such, the mean profile width (horizontal bars) is considered a more robust measure and will be used frequently in later sections.

In terms of updraught widths, simulations with a 200-m grid length show the closest agreement with the observations, although the updraught strength is underestimated in the mid-to-upper troposphere. In terms of reflectivity however, the mean 20-dBZ profile widths in the observations are closest to those in the 500-m grid length simulations while the mean profiles (colour profiles) more closely resemble the 200-m grid length simulations. Typical convective

mass fluxes based on these updraught profiles in the mid-troposphere for 500-m and 1.5-km grid length simulations are an order of magnitude larger than those derived from the radar observations.

A similar analysis to that presented in Fig. 7 has been performed with a simple but important difference. In addition to setting the velocity and reflectivity profiles to zero when they pass below a given threshold (e.g. 1 m s^{-1} and 20 dBZ), they are now also set to zero beyond any point where the profile increases with distance away from the profile maximum. This condition requires that each profile decreases monotonically from the maximum value and the resulting profiles may be considered to be 'primary profiles'. That is, we now exclude any secondary peaks in the individual horizontal profiles. The resulting mean profiles are shown in Fig. 8. This condition has little effect on the vertical velocity profiles, but significant differences can be observed in terms of reflectivity, particularly in the observations. Now, simulations with a 200-m grid length have the closest agreement with the observations in terms of updraught and reflectivity core width.

In Fig. 9a, the mean profile widths of the updraughts are shown versus the mean profile widths of the reflectivity cores, corresponding to the data in Fig. 7 for the height interval from 2.75 to 3 km. The error bars indicate the standard deviations of both the updraught and reflectivity profile widths. The widths of the corresponding primary profiles are shown in Fig. 9b., relating to Fig. 8. The profile widths and primary profile widths at the same height for the 'shallow' case (20 April 2012) are shown in Fig 9c and 9d. A clear relationship between updraught and reflectivity profile width is apparent when considering the primary profiles. These results suggest that the primary profile width in terms of reflectivity may be used as a proxy for the updraught width. Both here

and more generally in Fig. 8, the agreement between the 200-m grid-length simulations and the observations in terms of the horizontal scale of the updraughts is exceptional.

Comparisons between the updraught and reflectivity profile widths show exactly the same trends at other heights and these trends were largely insensitive to changes in the reflectivity threshold. Updraught widths obtained from the scaled, single component of convergence estimates based on the 500-m simulations were found to be underestimated by approximately 25 % in comparison with the widths obtained from the true model vertical velocity cross-sections. This suggests that the radar-derived updraught widths are also likely to be similarly underestimated, though does not significantly change the interpretation of the results presented.

The biggest difference between the 'profile widths' and the 'primary profile widths' occurs for the reflectivity profiles in the observations and in the highest resolution model simulations. The difference between the profile and primary profile widths in terms of reflectivity is close to a factor 3 in the observations and for simulations with a 100-m grid length. These factors are closer to 2, 1.5 and 1.2 in the 200-m, 500-m and 1500-m grid length simulations. Particularly at larger grid lengths, simulated precipitation patterns tend to be overly smooth and isolated.

4.2 Influence of sub-grid mixing length

We now consider the influence of the mixing length in the sub-grid turbulent mixing scheme on the scale of updraught and reflectivity profile widths focusing on simulations with 200-m and 500-m grid lengths. As in Fig. 9, Fig. 10 depicts the updraught profile widths versus reflectivity profile widths (left column) on 25 August 2012 for the same height interval (2.75-3 km) and similarly for the primary profiles (right column). Mixing lengths of 40 m, 100 m and 300 m have been considered for model simulations with grid lengths of 500 m (top row) and 200 m (bottom

row). The effect of increasing mixing length is generally to increase the scale of both the updraught and reflectivity cores, approximately in proportion to each other. Although the best agreement in terms of the reflectivity profile width at both grid lengths is shown for the 300-m mixing length, the horizontal scale and intensity (not shown) of the updraughts are significantly overestimated in these simulations. In terms of updraft scale, the closest match relates to the 40-m mixing length simulations, in agreement with the primary reflectivity profile widths.

4.3 Influence of microphysical parameterisation

Due to computing constraints, only a limited number of simulations have been performed investigating the influence of microphysical parameterisations. In addition to the default configuration using a 200-m grid length, two further simulations have been undertaken for the deep storm case: one with the inclusion of prognostic graupel and the other treating all ice as aggregates, rather than applying a diagnostic separation between crystals and aggregates (see Stein *et al*. 2014 for further details). These results are shown in Fig. 11, again in terms of profile and primary profile widths, and this time at heights of 3 km (top row) and 2 km (bottom row). Although the updraught and reflectivity core widths are very similar considering the primary profiles, some degree of broadening is observed in the reflectivity profile widths for the 'all-aggregate' simulations and even more so for the 'graupel' simulations. As the same trend is observed both above (3-km height) and below (2-km height) the 0° C isotherm (~2.6-km height), the differences cannot be explained by changes in reflectivity due to changes in precipitation class (e.g. ice crystals, aggregates or graupel). The wider reflectivity profile widths in these cases may be related to the increase in particle fall speeds, resulting in less diffuse precipitation fields. In the absence of a full bin microphysical treatment, the increase in particle fall speed in the ice phase appears to produce more realistic horizontal reflectivity profiles.

5. CONCLUSIONS

A novel technique for the estimation of updraught size and strength in convective rain cells has been developed for use on single-Doppler RHI scans. This involved a weighted average of vertical velocity estimates based on the ground-up and top-down integration of observed convergence. This approach has been applied to model data at a grid length corresponding to the radar observations to determine the appropriate scaling of estimates based on a single component of the horizontal convergence. Though the scaling of these estimates may not be accurate on a cell-by-cell basis, it is intended to improve the quality of the estimates in a statistical sense. While better estimates are likely to be obtained for individual storms from dual- or multiple Doppler analyses, the approach described allows information to be derived from single-Doppler observations, which are far more prevalent. The compositing of a large number of storms has been made to mitigate random errors inherent in this approach for individual retrievals.

Generally, it has been found that the representation of the horizontal scale of updraughts in the UM tends to decrease, though not linearly, with grid length. Progressively at sub-kilometre grid lengths, the horizontal updraught scale was largely determined by the mixing length in the sub-grid turbulence scheme rather than by the grid length *per se*. The 200-m grid length simulations showed the closest correspondence with the radar observations in terms of the horizontal scale of the convective updraughts. The updraughts in the 100-m grid length simulations tended to be narrower, which may be due to insufficient mixing in the sub-grid turbulence scheme.

The mixing length has typically been set at 0.2 times the horizontal grid length in UM simulations. This was derived for Large Eddy Models (LEM) making assumptions about the resolved turbulence. The observed differences between the 100-m and 200-m grid length

simulations may be influenced by the semi-Lagrangian dynamics in the UM (rather than the Eulerian framework used in LEM). Insufficient vertical resolution in relation to the very high horizontal resolution in the 100-m simulations may also contribute to insufficient mixing in the mid troposphere, where the grid boxes are vertically elongated. The results presented suggest that a lower limit of ~ 40 m could be used to maintain the simulated updraughts at a correct horizontal scale in very high resolution simulations. Alternatively, it is implied that the benefits of running simulations with grid lengths below 200 m may have only marginal benefits considering the significant increase in computational cost.

In general, simulated updraughts tended to weaken above the 0° C isotherm, through the mid-troposphere in contrast with those derived from the radar observations. Future work will consider the effects of increasing the vertical resolution and the mixing length in the 100-m grid length simulations, and allowing the mixing length to vary as a function of altitude. Subsequently, more detailed studies on the role of microphysical parameterizations will be undertaken.

The observations indicate that while horizontal reflectivity (or precipitation) profiles often do not decrease monotonically from their peak (i.e. these profiles often have secondary peaks), updraught profiles do decrease monotonically from the maximum values and their widths correspond to those of the primary reflectivity profiles (defined to be monotonically decreasing). If the reflectivity profiles are not required to decrease monotonically, rain cells appear to be larger than the reflectivity cores (primary peaks) by about a factor 3 based on radar observations from two distinct case studies considered here. The multi-peaked profiles observed in the radar data do not appear to be represented in simulated reflectivity profiles, except at the highest resolution considered (100-m grid length) with default configurations. This could be related to better resolved air motions at higher spatial resolutions which allow a form of drop sorting and

redistribution even though the simulations used a single-moment microphysics scheme. Typically in the UM, reflectivity profiles tend to decrease monotonically from their peak values, resulting in relatively smooth and isolated rain cells compared to observations. However, the inclusion of prognostic graupel in the 200-m grid length simulations improves the correspondence with observations in this respect.

Previous studies from the DYMECS project have been based on the analysis of storm morphology and rain cell dimensions based on surface rain rates presented by Stein *et al*. (2014) and Hanley *et al*. (2014) respectively. In these papers, storms represented in simulations with a 200-m grid length were typically narrower and surface rain cells smaller in comparison with observations for 'large storm' cases. In general, closer agreement was found with simulations using a 500-m grid length. It has been determined that increasing the mixing length with sub 1-km grid lengths leads to proportionally wider reflectivity *and* updraught profiles. Increased mixing has been shown to produce more realistically sized surface rainfall patterns (Hanley *et al*., 2014) in 200-m grid length runs of the UM in some cases. However, the results here imply that this would also lead to updraughts that are too broad and intense; the precipitation totals from individual convective cells would be excessively large. Hanley *et al.* (2014) found that the domain-averaged rainfall was not greatly influenced by grid length or mixing length settings. This suggests that updraughts that are significantly too intense would also be too few, and the spatial distribution of rainfall may not faithfully represent reality.

Acknowledgements

We would like to acknowledge that the DYMECS project was funded by NERC (grant NE/I009965/1) and that the National Centre for Atmospheric Science has supported this work.

We would also like to thank Darcy Ladd, Alan Doo, Chris Walden and Mal Clarke at the Chilbolton Facility for Atmospheric Radar Research (CFARR) for their perpetual willingness to provide assistance. We acknowledge use of the MONSooN system, a collaborative facility supplied under the Joint Weather and Climate Research Programme, which is a strategic partnership between the Met Office and the Natural Environment Research Council.

References

Baldauf M, Seifert A, Foerstner J, Majewski D, Raschendorfer M, Reinhardt T. 2011. Operational convective-scale numerical weather prediction with the COSMO model: Description and sensitivities. *Mon. Wea. Rev.*, **139**, 3887-3905.

Bousquet O, Chong M. 1998. A multiple-Doppler synthesis and continuity adjustment technique (MUSCAT) to recover wind components from Doppler radar measurements. *J. Atmos. Oceanic Technol.*, **15**, 343-359.

Browning KA, Roberts NM, Illingworth AJ. 1997. Mesoscale analysis of the activation of a cold front during cyclogenesis. Q*uart. J. Roy. Meteor. Soc.,* **123**, 2349-2375.

Browning KA, Marsham J, Nicol JC, Perry F, White B, Blyth A, Mobbs S. 2010. Observations of slantwise circulations above a cool undercurrent in a mesoscale convective system. *Quart. J. Royal Meteorol. Soc*., **135**, 354–373.

Bryan GH, Morrison H. 2012. Sensitivity of a simulated squall line to horizontal resolution and parameterization of microphysics. *Mon. Wea. Rev.*, **140**, 202-225.

Caine S, Lane TP, May PT, Jakob C, Siems ST, Manton MJ, Pinto J. 2013. Statistical assessment of tropical convection-permitting model simulations using a cell-tracking algorithm. *Mon. Wea. Rev.*, **141**, 557-581.

Chapman D, Browning KA. 1998. Use of wind-shear displays for Doppler radar data. *Bull. Amer. Met. Soc.*, **79**, 2685-2691.

Charney JG, Phillips NA. 1953. Numerical Integration of the quasi-geostrophic equations for barotropic and simple baroclinic flows. *J. Meteor.*, **10**, 71-99.

Collis S, Protat A, May PT, Williams C. 2013. Statistics of storm updraught velocities from TWP-ICE including verification with profiling measurements. *J. Appl. Meteor. Clim.*, **52**, 1909-1922.

Crosier J, Choularton T, Westbrook C, Blyth A, Bower K, Connolly P, Dearden C, Gallagher M, Cui Z, Nicol JC. 2013. Microphysical properties of cold frontal rainbands. *Quart. J. Royal Meteorol. Soc*., **140**, 1257-1268.

Davies T, Cullen MJP, Malcolm AJ, Mawson MH, Staniforth A, White AA, Wood N. 2005. A new dynamical core for the Met Office's global and regional modeling of the atmosphere. Q*uart. J. Roy. Meteor. Soc.,* **131**, 1759-1782.

Gao J, Xue M, Shapiro A, Droegemeier KK. 1999. A variational method for the analysis of three-dimensional wind fields from two Doppler radars. *Mon. Wea. Rev.*, **127**, 2128-2142.

Goddard JWF, Eastment JD, Thurai M. 1994a. The Chilbolton advanced meteorological radar: A tool for multidisciplinary research. *Electr. Commun. Eng. J*., 6, 77-86.

Goddard JWF, Tan J, Thurai M. 1994b. Technique for calibration of meteorological radars using differential phase. *Electronic Letters*, **30**, 166-167.

Halliwell C. 2007. Unified Model Documentation Paper 28: Subgrid turbulence scheme. Technical Report, Met Office.

Hanley KE, Plant RS, Stein THM, Hogan RJ, Nicol JC, Lean HW, Halliwell CE, Clark PA. 2014. Mixing length controls on high resolution simulations of convective storms. *Quart. J. Royal Meteorol. Soc*., DOI: 10.1002/qj.2356.

Kain JS, Weiss SJ, Bright DR, Baldwin ME, Levit JJ, Carbin GW, Schwartz CS, Weisman ML, Drogemeier K, Weber DB, Thomas KW. 2008. Some practical considerations regarding horizontal resolution in the first generation of operational convection-allowing NWP. *Wea. Forecasting*, **23**, 931-952.

Lean HW, Clark PA, Dixon M, Roberts NM, Fitch A, Forbes R, Halliwell C. 2008. Characteristics of high-resolution versions of the Met Office Unified Model for forecasting convection over the United Kingdom. *Mon. Wea. Rev.*, **136**, 3408-3424.

Lilly DK. 1967. The representation of small-scale turbulence in numerical simulation experiments. *Proc 10th Scientific Computing Symp. On Environmental Sciences*, Yorktown Heights, NY, IBM, 195-210.

McBeath K, Field PR, Cotton RJ. 2013. Using operational weather radar to assess high-resolution numerical weather prediction over the British Isles for a cold air outbreak case-study. *Quart. J. Royal Meteorol. Soc*., **140**, 225-239.

May PT, Rajopadhyaya DK. 1999. Vertical velocity characteristics of deep convection over Darwin, Australia. *Mon. Wea. Rev.*, **127**, 1056-1071.

Miller LJ, Strauch RG. 1974. A dual-Doppler radar method for the determination of wind velocities within precipitating weather systems. *Remote Sens. Environ.*, **3**, 219-235.

Protat A, Zawadzki I. 1999. A variational method for real-time retrieval of three-dimensional wind field from multiple-Doppler bistatic radar network data. *J. Atmos. Oceanic Technol.*, **16**, 432-449.

Ray PS, Ziegler CL, Bumgarner W, Serafin RJ. 1980. Single and multiple Doppler radar observations of tornadic storms. *Mon. Wea. Rev.*, **108**, 1607-1625.

Scialom G, Lemaitre Y. 1990. A new analysis for the retrieval of three-dimensional mesoscale wind fields from multiple Doppler radar. *J. Atmos. Oceanic Technol.*, **7**, 640-665.

Smagorinsky J. 1963. General circulation experiments with the primitive equations. I: The basic experiment. *Mon. Wea. Rev.*, **91**, 99-164.

Stein THM, Hogan RJ, Clark PA, Halliwell CE, Hanley KE, Lean HW, Nicol JC, Plant RS. 2014. The DYMECS project: A statistical approach for the evaluation of convective storms in high-resolution NWP models. *Bull. Amer. Meteor. Soc.*, in review.

Stein THM, Hogan RJ, Hanley KE, Nicol JC, Lean HW, Plant RS, Clark PA, Halliwell CE. 2014. The three-dimensional morphology of simulated and observed convective storms over southern England. *Mon. Weather Rev.,* DOI: 10.1175/MWR-D-13-00372.1.

Varble A, Fridland AM, Zipser EJ, Ackerman AS, Chaboureau J-P, Fan J, Hill A, McFarlane SA, Pinty J-P, Shipway B. 2011. Evaluation of cloud-resolving model intercomparison

simulations using TWP-ICE observations: Precipitation and cloud structure. *J. Geophys. Res.*, **116**, D12206.

Weisman ML, Skamarock WC, Klemp JB. 1997. The resolution dependence of explicitly modeled convective systems. *Mon. Wea. Rev.*, **125**, 527-548.

Wilson DR, Ballard SP. 1999. A microphysically based precipitation scheme for the UK meteorological office unified model. *Quart. J. Royal Meteorol. Soc*., **125**, 1607-1636.

Figure Captions

Fig. 1. (a) Normalised weighting coefficients for the top-down (dotted trace) and ground-up (dashed trace) integration of horizontal convergence as a function of height; shown here for each kilometre of echo-top height (ETH) between 1 and 12 km based on the propagation of constant errors through a standard atmospheric density profile. (b) Vertical velocity estimation errors (normalized by the maximum value using the error-weighted approach) as a function of height with ETH = 12km for top-down and ground-up integrations; also shown for the linear-weighted (solid grey trace; Protat and Zawadzki, 1999) and error-weighted (solid black trace; based on Eq. 4) averages.

Fig. 2. Frequency Density Functions (FDF) (logarithmic units) of estimated vertical velocities based on a single component of the horizontal convergence in the 500-m grid length UM between 1200 and 1600 UTC on 25 August 2012, normalized as a function of altitude: (a) integrated down from the –5 dBZ echo-top, (b) integrated up from 500 m above the surface and (c) the weighted average of these estimates. FDFs of the actual vertical velocity in the UM are shown in (d). All FDFs correspond to cross-sections through the centre of the storms considered.

Fig. 3. (a) Cumulative frequency density functions of the actual vertical velocity (ms^{-1}) in the model (grey dashed trace) for the height interval from 6 to 6.25 km and for estimates based on a single component of convergence (grey solid trace). The scaling relationship between these functions is in shown in black. (b) Frequency density functions (logarithmic units) of model vertical velocity (black) showing the actual values (solid trace) and single-component estimates (dashed trace) for the same height interval. Corresponding radar observations (grey) using a single-component of convergence (dashed trace) and the best estimate of the true FDF after scaling using the relationship shown in (a).

Fig. 4. FDFs (logarithmic units) of estimated vertical velocities based on a single component of the horizontal convergence in the radar observations between 1200 and 1600 UTC on 25 August 2012, normalized as a function of altitude: (a) integrated down from the –5 dBZ echo-top, (b) integrated up from the lowest available elevation and (c) the weighted average of these estimates. FDFs of the scaled vertical velocity estimates are shown in (d). Radar observations were restricted to maximum range of 90 km.

Fig. 5. A vertical velocity retrieval (a) from an RHI at 1237 UTC 25 August 2012 and corresponding reflectivity image (b) regridded to 250-m height and 500-m range intervals.

Fig. 6. Average magnitude of vertical velocities (ms^{-1}) at the updraught centre (left column) and corresponding reflectivity profiles (middle column) as a function of height for 25 August 2012 (top row) and 20 April 2012 (bottom row). The number of updraught detections included in the averages at each height is also shown (right column).

Fig. 7. Mean horizontal profiles of vertical velocity (left column) and reflectivity (right column) from radar observations (top row) and as a function of model grid length between 1200 and 1600 UTC 25 August 2012. Model grid lengths are 1500m (second row), 500m (third row), 200m (fourth row) and 100m (final row). Profiles are set to zero beyond the 1 m s^{-1} and 20 dBZ contours for vertical velocity and reflectivity respectively. Black traces indicate the mean of the individual profile widths.

Fig. 8. As Fig. 7, but profiles are set to zero beyond the 1 m s^{-1} and 20 dBZ contours for vertical velocity and reflectivity respectively or beyond the point at which the profiles increase with distance away from the maximum.

Fig. 9. Mean horizontal profile widths (left column) of updraught velocity (> 1 m s^{-1}) versus reflectivity (> 20 dBZ) for 1500-m (blue), 500-m (cyan) 200-m (green) and 100-m (red) grid-length simulations and observations (black) between 1200 and 1600 UTC 25 August 2012 (top row) and between 1100 and 1600 UTC 20 April 2012 (bottom row) for 2.75-3 km height interval. The corresponding primary profile widths are also shown (right column). Error bars indicate the standard deviation of core widths.

Fig. 10. As Fig. 9, but for 500-m (top row) and 200-m (bottom row) grid-length simulations with mixing lengths of 40 m (green), 100 m (cyan) and 300 m (blue) and for observations (black) between 1200 and 1600 UTC 25 August 2012 for 2.75-3 km height interval.

Fig. 11. As Fig. 9, but for 200-m grid-length simulations with default settings (green), the inclusion of prognostic graupel (cyan) and an all-aggregate ice phase (blue) and for observations (black) between 1200 and 1600 UTC 25 August 2012 at heights of 2 km (top row) and 3 km (bottom row). The corresponding primary profile widths are also shown (right column). Error bars indicate the standard deviation of core widths.

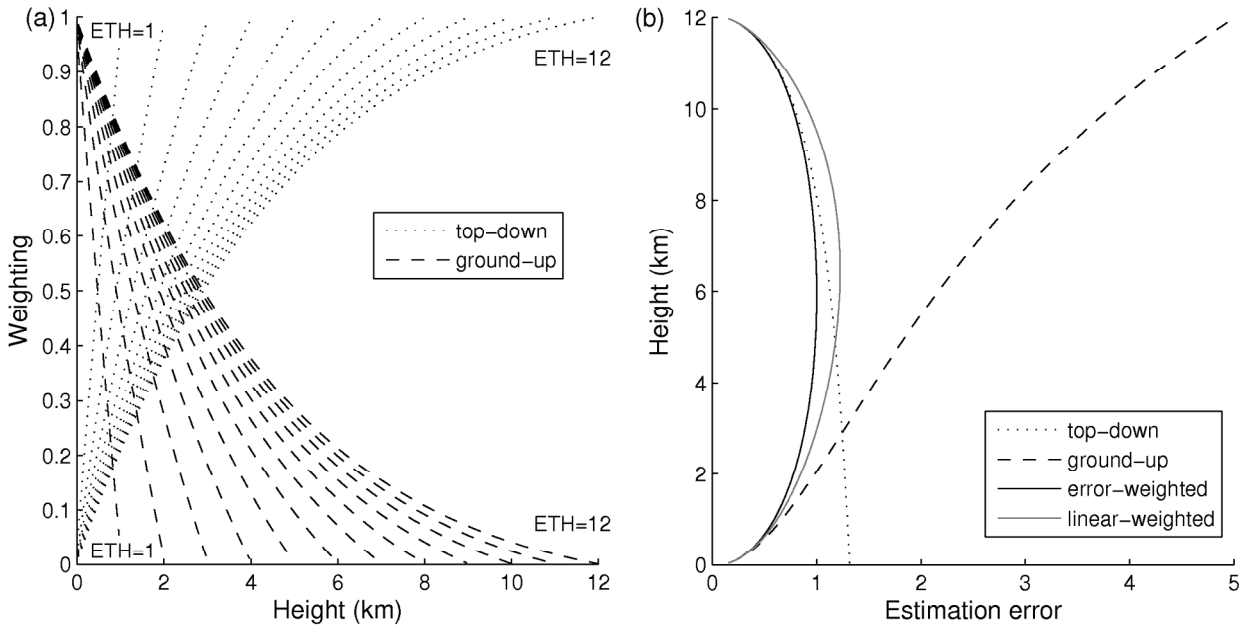

Fig. 1. (a) Normalised weighting coefficients for the top-down (dotted trace) and ground-up (dashed trace) integration of horizontal convergence as a function of height; shown here for each kilometre of echo-top height (ETH) between 1 and 12 km based on the propagation of constant errors through a standard atmospheric density profile. (b) Vertical velocity estimation errors (normalized by the maximum value using the error-weighted approach) as a function of height with ETH = 12km for top-down and ground-up integrations; also shown for the linear-weighted (solid grey trace; Protat and Zawadzki, 1999) and error-weighted (solid black trace; based on Eq. 4) averages.

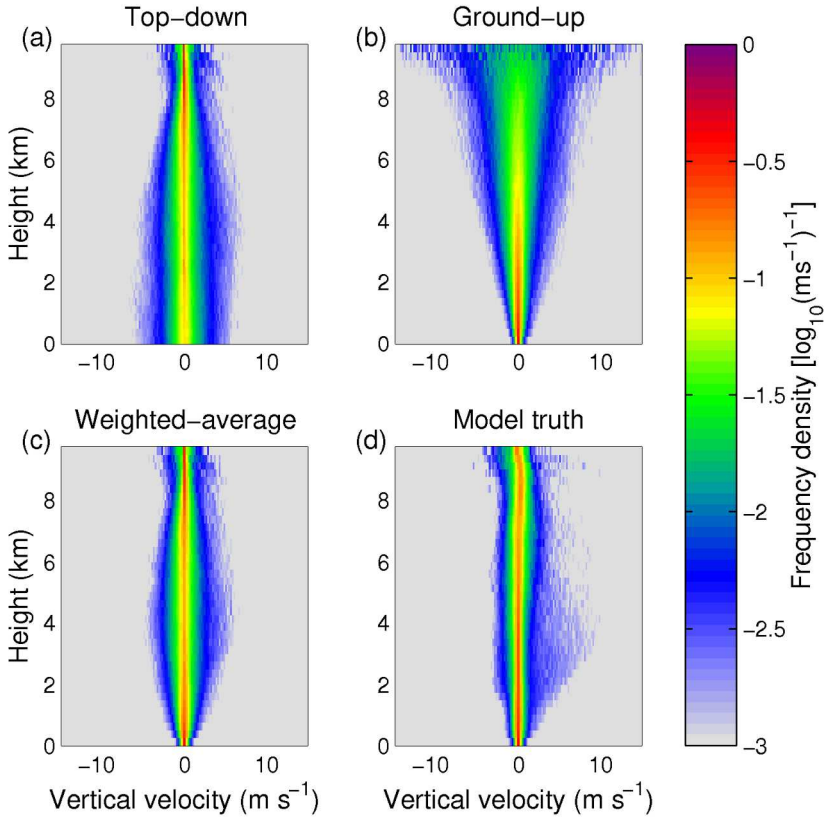

Fig. 2. Frequency Density Functions (FDF) (logarithmic units) of estimated vertical velocities based on a single component of the horizontal convergence in the 500-m grid length UM between 1200 and 1600 UTC on 25 August 2012, normalized as a function of altitude: (a) integrated down from the –5 dBZ echo-top, (b) integrated up from 500 m above the surface and (c) the weighted average of these estimates. FDFs of the actual vertical velocity in the UM are shown in (d). All FDFs correspond to cross-sections through the centre of the storms considered.

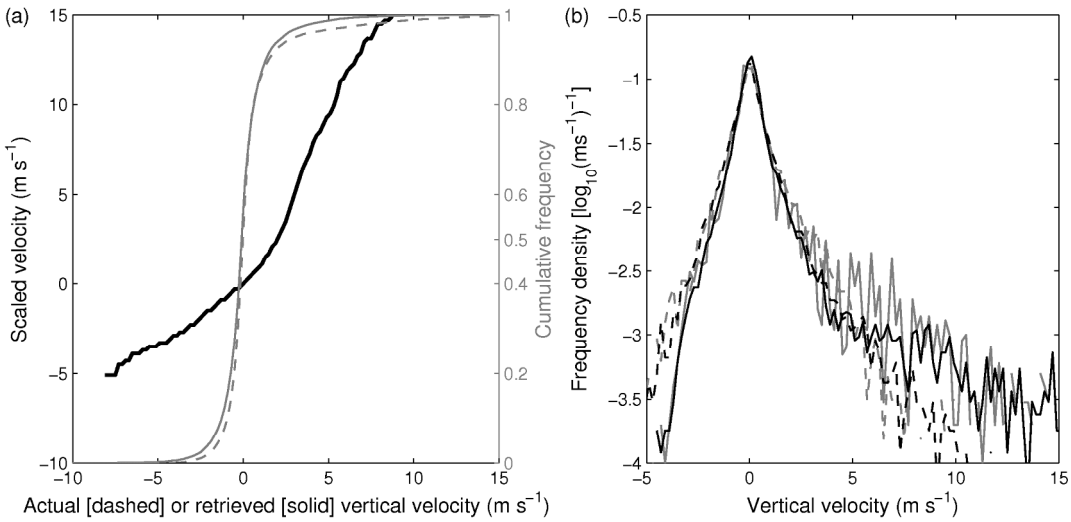

Fig. 3. (a) Cumulative frequency density functions of the actual vertical velocity (ms^{-1}) in the model (grey dashed trace) for the height interval from 6 to 6.25 km and for estimates based on a single component of convergence (grey solid trace). The scaling relationship between these functions is in shown in black. (b) Frequency density functions (logarithmic units) of model vertical velocity (black) showing the actual values (solid trace) and single-component estimates (dashed trace) for the same height interval. Corresponding radar observations (grey) using a single-component of convergence (dashed trace) and the best estimate of the true FDF after scaling using the relationship shown in (a).

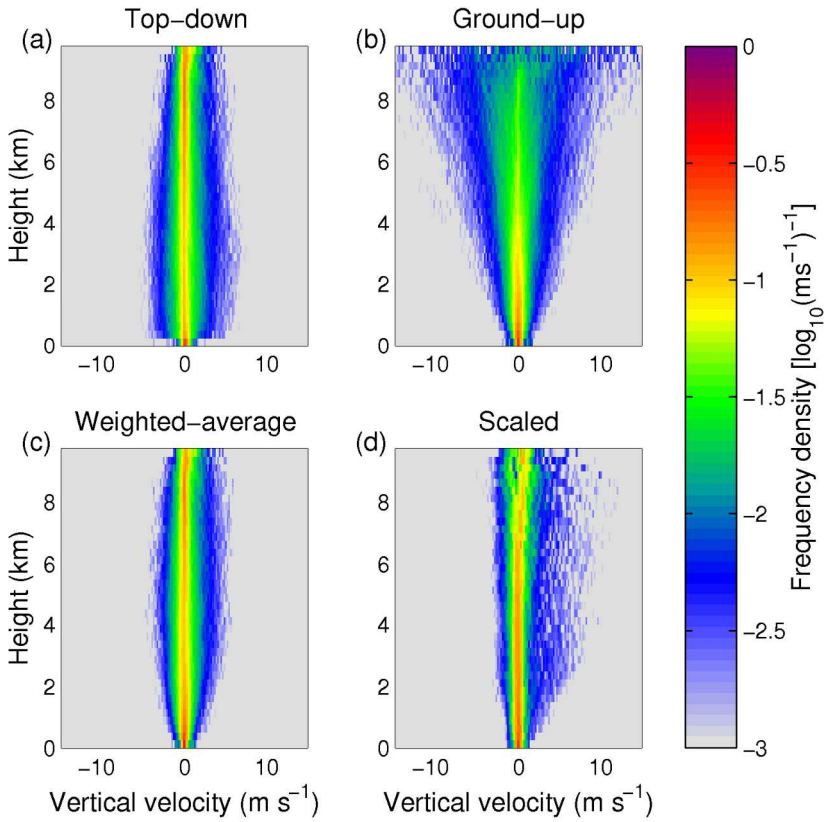

Fig. 4. FDFs (logarithmic units) of estimated vertical velocities based on a single component of the horizontal convergence in the radar observations between 1200 and 1600 UTC on 25 August 2012, normalized as a function of altitude: (a) integrated down from the –5 dBZ echo-top, (b) integrated up from the lowest available elevation and (c) the weighted average of these estimates. FDFs of the scaled vertical velocity estimates are shown in (d). Radar observations were restricted to maximum range of 90 km.

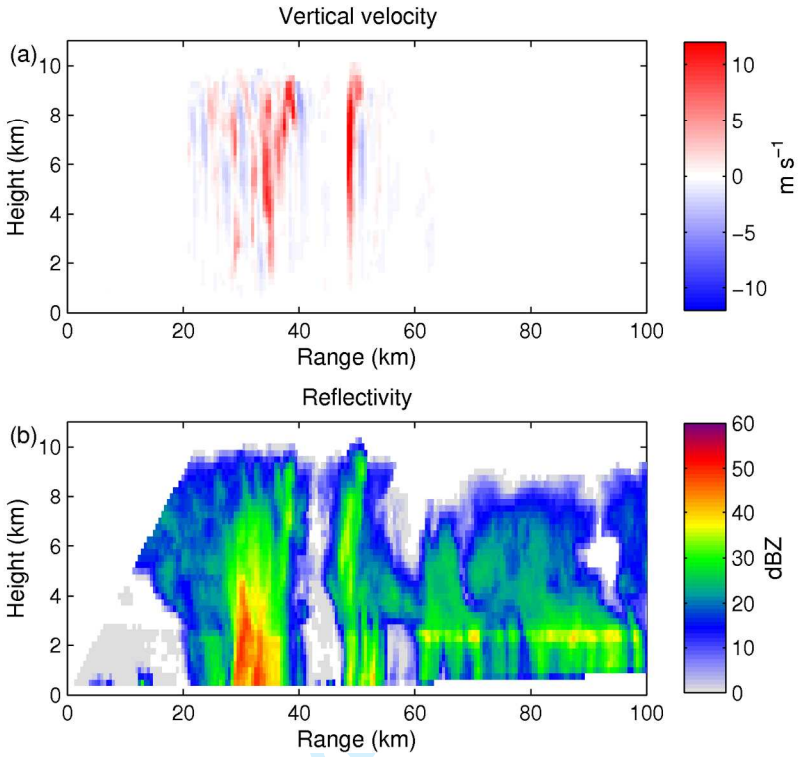

Fig. 5. A vertical velocity retrieval (a) from an RHI at 1237 UTC 25 August 2012 and corresponding reflectivity image (b) regridded to 250-m height and 500-m range intervals.

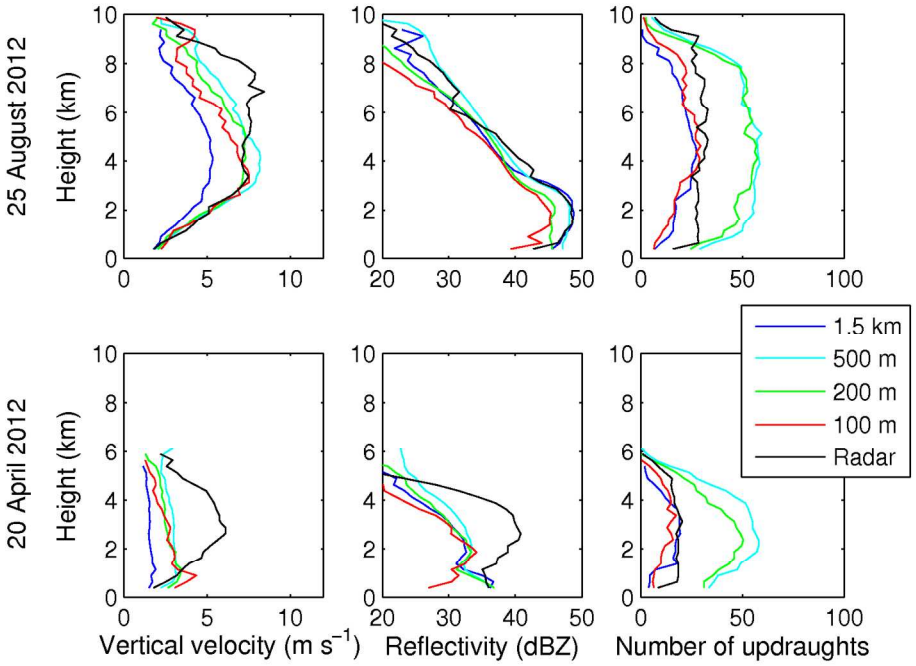

Fig. 6. Average magnitude of vertical velocities (ms^{-1}) at the updraught centre (left column) and corresponding reflectivity profiles (middle column) as a function of height for 25 August 2012 (top row) and 20 April 2012 (bottom row). The number of updraught detections included in the averages at each height is also shown (right column).

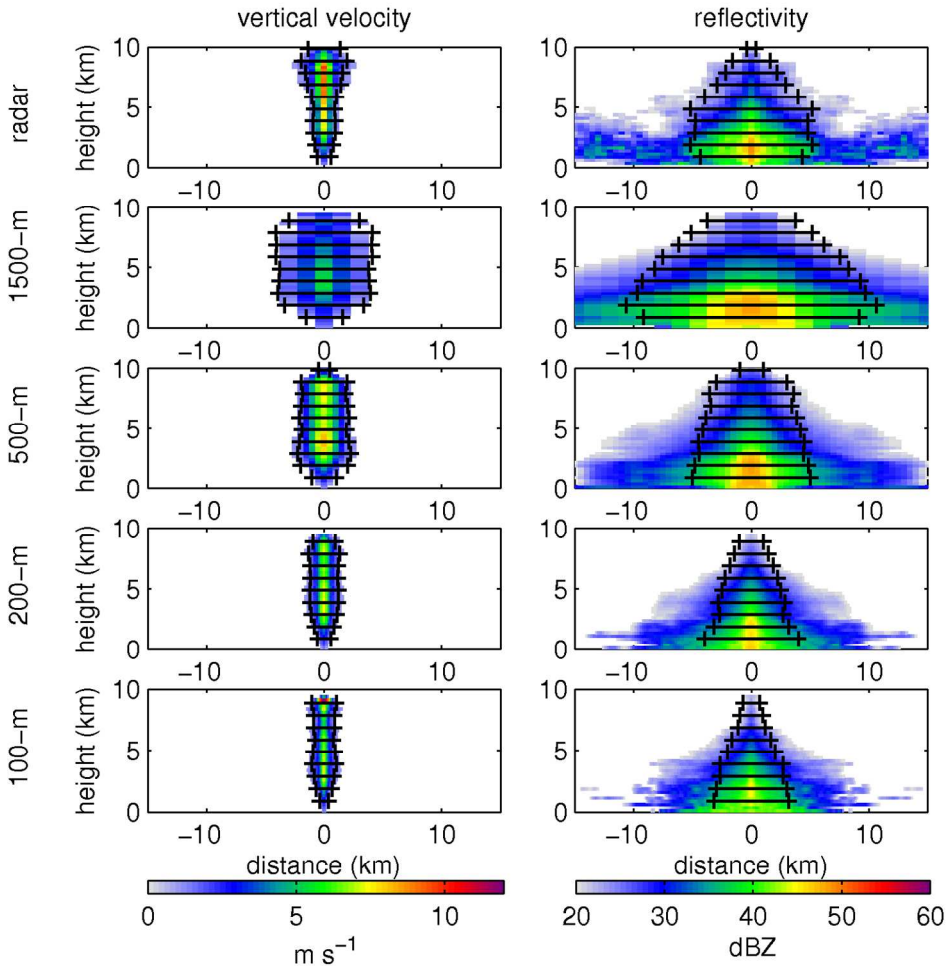

Fig. 7. Mean horizontal profiles of vertical velocity (left column) and reflectivity (right column) from radar observations (top row) and as a function of model grid length between 1200 and 1600 UTC 25 August 2012. Model grid lengths are 1500m (second row), 500m (third row), 200m (fourth row) and 100m (final row). Profiles are set to zero beyond the 1 m s $^{-1}$ and 20 dBZ contours for vertical velocity and reflectivity respectively. Black traces indicate the mean of the individual profile widths.

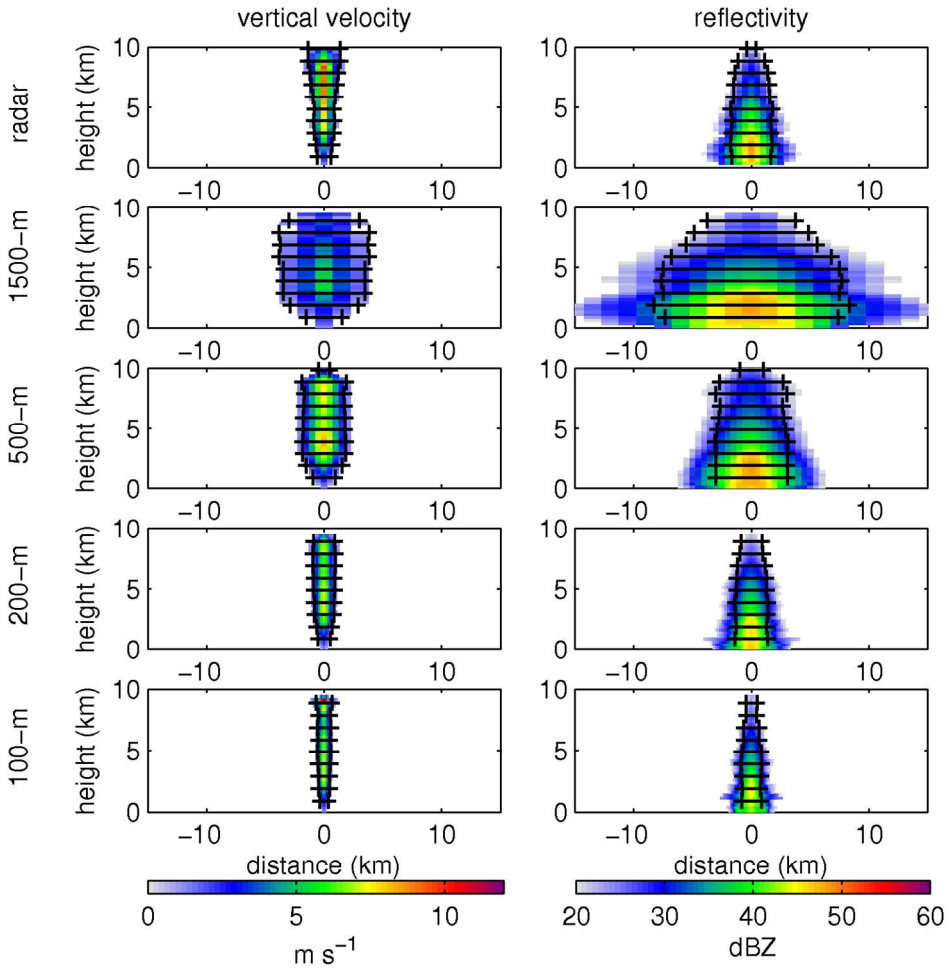

Fig. 8. As Fig. 7, but profiles are set to zero beyond the 1 m s $^{-1}$ and 20 dBZ contours for vertical velocity and reflectivity respectively or beyond the point at which the profiles increase with distance away from the maximum.

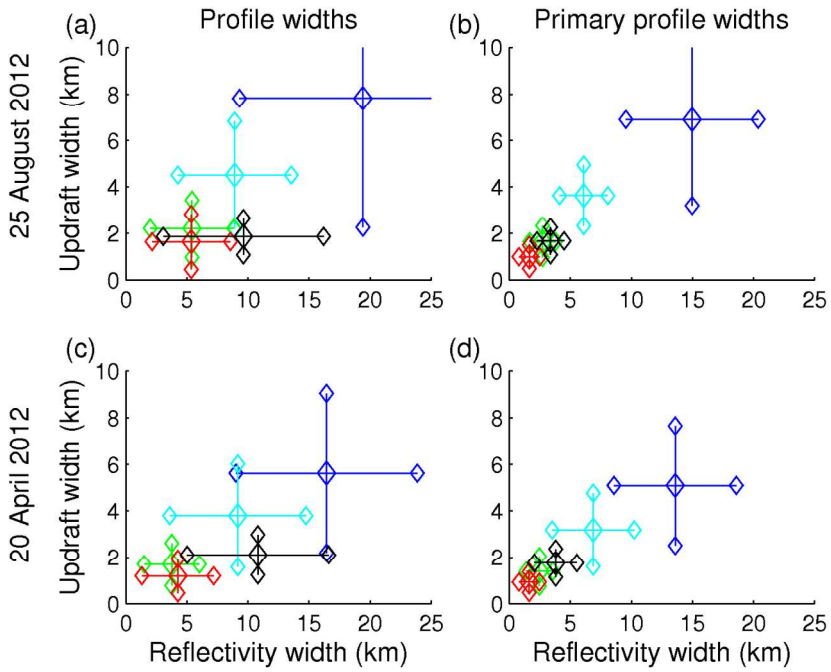

Fig. 9. Mean horizontal profile widths (left column) of updraught velocity (> 1 m s^{-1}) versus reflectivity (> 20 dBZ) for 1500-m (blue), 500-m (cyan) 200-m (green) and 100-m (red) grid-length simulations and observations (black) between 1200 and 1600 UTC 25 August 2012 (top row) and between 1100 and 1600 UTC 20 April 2012 (bottom row) for 2.75-3 km height interval. The corresponding primary profile widths are also shown (right column). Error bars indicate the standard deviation of core widths.

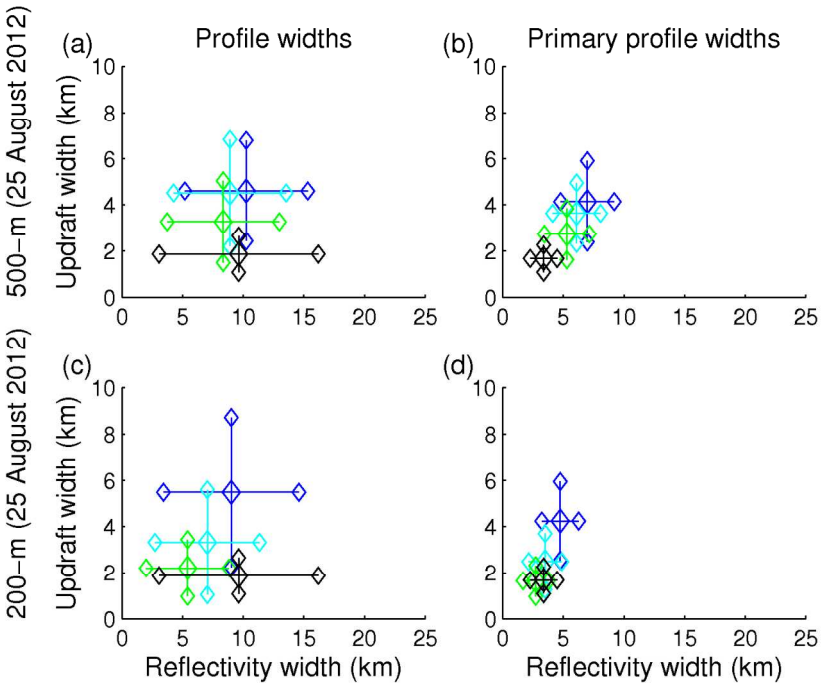

Fig. 10. As Fig. 9, but for 500-m (top row) and 200-m (bottom row) grid-length simulations with mixing lengths of 40 m (green), 100 m (cyan) and 300 m (blue) and for observations (black) between 1200 and 1600 UTC 25 August 2012 for 2.75-3 km height interval.

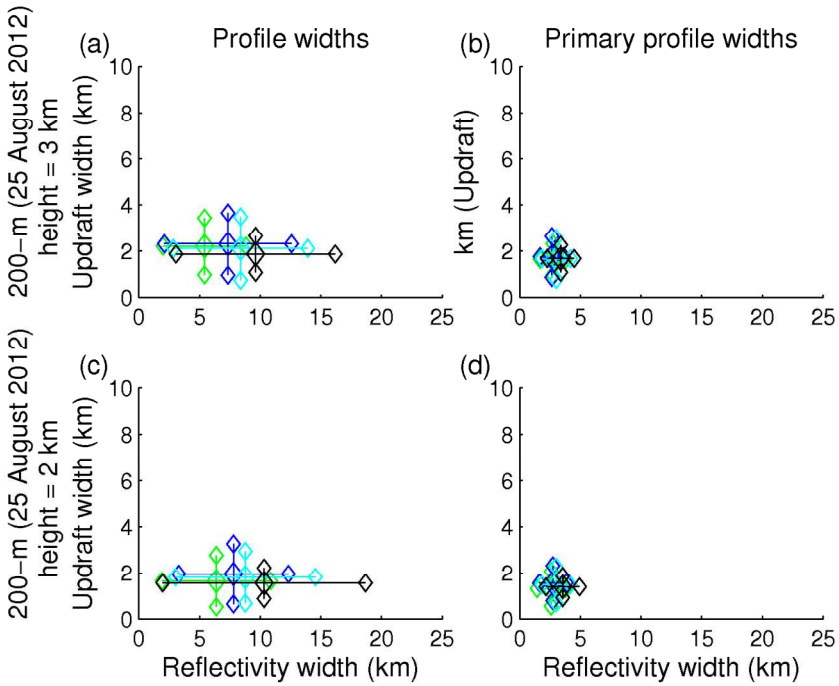

Fig. 11. As Fig. 9, but for 200-m grid-length simulations with default settings (green), the inclusion of prognostic graupel (cyan) and an all-aggregate ice phase (blue) and for observations (black) between 1200 and 1600 UTC 25 August 2012 at heights of 2 km (top row) and 3 km (bottom row). The corresponding primary profile widths are also shown (right column). Error bars indicate the standard deviation of core widths.